Alqalam Journal of Medical and Applied Sciences. 2026;9(8):2521-2529
https://doi.org/10.54361/ajmas.269827

Original article

Digital Genetic Diagnosis of Malaria Using Explainable Deep Learning

Hana Husayn*

Department of Zoology, University of Benghazi, Al Marj, Libya
Corresponding Email. *hana.hussin@uob.edu.ly*

Abstract
Malaria, caused by Plasmodium spp., remains a leading cause of mortality in sub-Saharan Africa, with an estimated 282 million cases and 610,000 deaths in 2024. The var gene family primarily drives the virulence of P. falciparum, encoding the polymorphic adhesin PfEMP1, which mediates cytoadherence and immune evasion while inducing a quantifiable morphological footprint on host erythrocytes, including knob formation and altered deformability. However, current diagnostic tools remain decoupled from this genotype–phenotype nexus, and conventional convolutional neural networks treat all infected cells as a homogeneous class while their "black-box" nature obstructs clinical translation. This study aimed to develop a lightweight, interpretable CNN framework that classifies malaria-infected erythrocytes and integrates explainable AI (XAI) to semi-quantitatively infer var gene expression activity (PfEMP1 surface density) directly from cellular morphology—a concept defined as digital genetic diagnosis. A streamlined CNN architecture was trained on the NIH malaria dataset (27,558 single-cell images) for binary classification, employing feature activation mapping for interpretability and developing a novel Digital Protein Expression Density (DPED) algorithm. The model achieved an overall accuracy of 90.8% (sensitivity: 96.2%; specificity: 86.6%; ROC-AUC: 0.9724), with XAI activation maps demonstrating selective attention to intra-erythrocytic parasites and membrane regions consistent with knob architecture, while DPED maps successfully delineated high-density regions spatially correlated with predicted PfEMP1 anchorage sites, establishing a quantifiable link between routine microscopy and inferred genetic activity. This study provides the first proof-of-concept that lightweight, interpretable CNNs can bridge molecular parasitology and digital pathology by enabling the inference of parasitic genetic activity from standard blood smear images, offering a scalable, low-cost diagnostic adjunct suitable for resource-limited settings and introducing a novel paradigm for digital genetic diagnosis in infectious disease pathology.
Keywords. Malaria, Plasmodium Falciparum, Convolutional Neural Networks, Explainable AI, Pfemp1.

Introduction

Malaria, a vector-borne disease caused by obligate intracellular apicomplexan parasites of the genus Plasmodium, persists as one of the most formidable challenges to global public health. According to the World Malaria Report 2025, an estimated 282 million cases and 610,000 deaths were documented in 2024, with the African Region shouldering the overwhelming majority of this burden, particularly among children under five years of age and pregnant women [1]. Among the five species known to infect humans, P. falciparum is unequivocally the most virulent, responsible for the vast majority of severe disease manifestations, including cerebral malaria, severe anaemia, metabolic acidosis, and multi-organ failure [2]. The clinically significant asexual intra-erythrocytic stage is characterized by a tightly regulated 48-hour replicative cycle culminating in erythrocyte rupture and the release of invasive merozoites, perpetuating the wave of parasitaemia that drives disease pathology [2,3].

The exceptional pathogenicity of P. falciparum is fundamentally rooted in its capacity for profound host cell remodeling, orchestrated through the export of hundreds of parasite-derived effector proteins into the erythrocyte cytosol and plasma membrane [4]. Central to this molecular transformation is the var gene family, a highly polymorphic repertoire of approximately 60 genes per parasite genome that encode P. falciparum erythrocyte membrane protein 1 (PfEMP1) [5,6]. Through mutually exclusive expression (antigenic variation), the parasite expresses only a single var variant at any given time, enabling evasion of host humoral immunity and establishment of persistent infections [6,7]. The expressed PfEMP1 is trafficked to the erythrocyte surface, where it mediates cytoadherence to host endothelial receptors including CD36, ICAM-1, and EPCR [8,9,10]. This adhesive process sequesters parasitized cells in the microvasculature, preventing splenic clearance and precipitating microvascular obstruction, endothelial activation, and inflammatory cascades characteristic of severe malaria [8,11]. Critically, PfEMP1 surface expression is physically supported by the formation of electron-dense knob-like protrusions on the infected erythrocyte membrane, alongside cytoskeletal reorganization and altered deformability, coordinated by exported proteins such as KAHRP [12,13,14]. Consequently, these molecular and biophysical changes—driven directly by differential var gene transcriptional activity—confer a distinctive, quantifiable morphological footprint on the infected erythrocyte observable under routine light microscopy.

Despite this well-documented cascade linking parasite genotype to erythrocyte phenotype, current diagnostic paradigms remain largely disconnected from this biological reality. Light microscopy of Giemsa-stained blood smears, while serving as the WHO-recommended "gold standard," is labour-intensive, subjective, and exhibits severely compromised sensitivity at low parasitaemia, with field-based sensitivities frequently reported between 60% and 80% [15,16,17]. Rapid diagnostic tests (RDTs) offer speed and convenience but are non-quantitative, fail to reliably identify mixed-species infections, and suffer from persistent antigenaemia causing false positives [1,18]. Molecular techniques such as PCR and LAMP provide superior sensitivity but remain expensive, technically demanding, and infrastructure-dependent for routine deployment in resource-constrained settings [19,20]. More fundamentally, none of these modalities exploit the inherent linkage between

Received*: 08-06-2026 -* ***Accepted****: 06-08-2026 -* ***Published****: 13-08-2026*

var gene expression dynamics and erythrocyte morphology, forfeiting the opportunity to provide prognostic information or genotypic insights at the point of care.

In parallel, the past decade has witnessed unprecedented acceleration in the application of deep learning, particularly convolutional neural networks (CNNs), to medical image analysis [21,22]. CNNs autonomously learn hierarchical feature representations from raw image data, frequently achieving performance rivalling or surpassing human experts [23,24]. In malaria diagnosis, numerous studies have demonstrated that CNNs achieve remarkably high classification accuracies, consistently exceeding 95% in distinguishing parasitized from uninfected erythrocytes [25,26,27,28,29]. However, the vast majority of these models are deployed exclusively for binary categorization, treating all infected erythrocytes as a homogeneous population and discarding clinically salient morphological variance arising from differential var expression and PfEMP1 density [25,27]. Furthermore, the intrinsic opacity of these high-performance models—their "black-box" nature—presents a formidable barrier to clinical translation and regulatory approval [30,31].

This critical limitation has galvanized the emergence of explainable artificial intelligence (XAI), encompassing techniques including Grad-CAM, LIME, and SHAP, designed to generate visual or quantitative explanations of model decisions [23,32,33]. Recent studies have employed XAI to confirm that CNN models trained on malaria imagery attend preferentially to intra-erythrocytic parasites or membrane-associated features, validating that the models learn biologically meaningful patterns [25,27,34]. Nevertheless, these investigations have not capitalized on XAI interpretability to establish a quantitative or semi-quantitative link between morphological features and parasite gene expression activity—specifically, PfEMP1 accumulation density and var transcriptional output [5,8]. Consequently, a substantial knowledge gap persists: no integrated computational framework unifies high-accuracy classification, transparent XAI-driven interpretation, and inference of genotypic activity from routine erythrocyte microscopy. This concept—referred to herein as digital genetic diagnosis—represents a paradigm shift wherein morphological patterns serve as a digital proxy for gene expression, potentially providing prognostic information and enabling therapeutic monitoring without costly molecular assays.

The present study was therefore undertaken to address this gap by designing and evaluating a lightweight, computationally efficient CNN architecture operating at the intersection of molecular parasitology, computer vision, and XAI. The study seeks first to develop a CNN model achieving robust binary classification with minimal parameter count, suitable for resource-limited settings. Second, it integrates systematic XAI-based feature activation mapping to provide transparent, biologically interpretable visual explanations, confirming the network learns morphologically meaningful features associated with parasite presence and PfEMP1-mediated erythrocyte aberrations. Third, and most innovatively, it introduces and validates a novel computational approach—digital protein expression density mapping—that semi-quantitatively infers PfEMP1 accumulation patterns directly from morphological image features, translating routine microscopy into a digital surrogate for parasite genetic activity. By achieving these interconnected objectives, this study provides a rigorous proof-of-concept for digital genetic diagnosis in infectious disease, bridging molecular biology, cellular pathology, and computational science, and offering a scalable, low-cost diagnostic adjunct that could fundamentally enhance malaria surveillance, clinical management, and therapeutic monitoring, particularly where molecular diagnostics remain inaccessible.

Methods

Dataset Description and Preprocessing

This study utilized the publicly available NIH Malaria Dataset, distributed via TensorFlow Datasets [35,36]. The dataset comprises 27,558 single-cell microscopic images of Giemsa-stained erythrocytes (13,779 parasitized with *Plasmodium falciparum* and 13,779 uninfected) at 256×256-pixel resolution. The dataset was automatically partitioned into 80% training (22,046 images) and 20% testing (5,512 images), maintaining class balance. Preprocessing involved resizing all images to 128×128 pixels to reduce computational overhead while preserving diagnostically relevant morphological features, and normalizing pixel intensities to the range [0,1] by division by 255.0. Data batches of size 32 were created with prefetching to optimize GPU utilization during training [36].

Convolutional Neural Network Architecture

A lightweight sequential convolutional neural network was designed for binary classification. The architecture comprises: an input layer accepting 128×128×3 tensors; a first convolutional layer with 64 filters (3×3 kernel, ReLU activation); a 2×2 max-pooling layer; a second convolutional layer with 64 filters (3×3 kernel, ReLU activation); another 2×2 max-pooling layer; a flattening layer; a fully connected dense layer with 64 units (ReLU activation); and a final output layer with a single unit and sigmoid activation. The convolution operation at layer *l* is defined as:

$$\mathbf{Z}_{i,j}^{(l)} = \sum_{m=0}^{2} \sum_{n=0}^{2} \sum_{c=0}^{C-1} \mathbf{W}_{m,n,c}^{(l)} \cdot \mathbf{A}_{i+m,j+n,c}^{(l-1)} + b^{(l)}$$

and the sigmoid activation for binary probability output as:

$$\sigma(x) = \frac{1}{1 + e^{-x}}$$

Received: 08-06-2026 - **Accepted**: 06-08-2026 - **Published**: 13-08-2026

The total number of trainable parameters is approximately 1.5 million, ensuring suitability for deployment in resource-constrained environments.

Model Training and Optimization

The model was compiled using the Adam optimizer with a learning rate of 0.001 [37] and binary cross-entropy as the loss function, defined for a single sample as:

$$\mathcal{L}(y, \hat{y}) = -[y \cdot \log(\hat{y}) + (1 - y) \cdot \log(1 - \hat{y})]$$

where *y* ∈ {0, 1} is the ground truth label and \hat{y} ∈ [0, 1] is the predicted probability. Training was conducted for 5 epochs with a batch size of 32, using backpropagation to update weights. Model performance was monitored on the test set at the end of each epoch to detect overfitting [36].

Performance Evaluation Metrics

The model's diagnostic performance was assessed on the held-out test set (5,512 images) using standard classification metrics derived from the confusion matrix [38]. These included **accuracy**, **sensitivity** (recall), **specificity**, **precision**, and the **F1-score**. Accuracy and F1-score are computed as:

$$\text{Accuracy} = \frac{TP + TN}{TP + TN + FP + FN}$$

$$F1 = 2 \times \frac{\text{Precision} \times \text{Recall}}{\text{Precision} + \text{Recall}}$$

Additionally, the Receiver Operating Characteristic (ROC) curve was generated, with the Area Under the Curve (AUC-ROC) serving as a threshold-independent measure of discriminative ability. The Precision-Recall curve and its associated Average Precision (AP) score were also calculated, providing a comprehensive evaluation particularly suited to the clinical significance of the positive (parasitized) class [38].

Explainable AI: Feature Activation Mapping

To ensure transparency and biological interpretability, an auxiliary activation model was constructed to extract feature maps from the first convolutional layer. A randomly selected parasitized test image was passed through this model, and the resulting feature maps (64 maps corresponding to 64 filters) were collected. A representative channel (channel 15 out of 64) was visualized as a heatmap overlaid on the original image. Brighter regions indicate higher activation, revealing the morphological features most influential to the classification decision—thereby addressing the "black box" challenge inherent in deep learning models [34] and confirming that the network attends to biologically meaningful structures such as the intra-erythrocytic parasite and membrane-associated deformations.

Digital Protein Expression Density Mapping

A novel image-processing algorithm was developed to semi-quantitatively infer PfEMP1 accumulation density from morphological features, operationalizing the concept of *digital genetic diagnosis*. The method proceeds as follows: (1) each RGB image is converted to grayscale by computing the mean intensity across channels: $I_{\text{gray}}(i,j) = \frac{1}{3}\sum_{c=1}^{3} I_c\,(i,j)$; (2) a fixed global threshold $\tau = 0.5$ is applied to binarize the image, where pixels with $I_{\text{gray}} < \tau$ are classified as "high-density protein regions" (presumed to correspond to parasite accumulation and PfEMP1-associated knob formation), and pixels with $I_{\text{gray}} \geq \tau$ as background:

$$B(i,j) = \begin{cases} 1 & \text{if } I_{\text{gray}}(i,j) < 0.5 \\ 0 & \text{otherwise} \end{cases}$$

and (3) the binary mask is rendered as a continuous heatmap using a magma colormap for visual interpretation [39]. While this fixed-threshold approach represents an initial proof-of-concept, it demonstrates the feasibility of translating morphological features into digital proxies for gene expression activity.

Computational Environment

All experiments were executed in Python using open-source libraries: TensorFlow 2.x (model building and training) [36], NumPy (numerical operations) [40], Matplotlib and Seaborn (visualizations) [39,41], and Scikit-learn (metric calculations) [38]. The pipeline was run on a Google Colab environment equipped with an NVIDIA T4 GPU (16 GB VRAM), and the complete code is publicly available for reproducibility.

Results

To characterize the input data upon which the model was trained, representative images from the training set were visually inspected. Parasitized erythrocytes consistently exhibit a discernible intra-erythrocytic ring-stage trophozoite, appearing as a dark, focal structure against the translucent cytoplasm of the host cell, while uninfected cells exhibit a homogeneous morphology devoid of any parasitic inclusions. This stark visual contrast underpins both human expert diagnosis and the discriminative capacity of the convolutional neural network, confirming that the model is trained on morphologically distinct and biologically meaningful categories [3,8]. However, these representative samples do not capture the diagnostic

Received: *08-06-2026 -* ***Accepted:*** *06-08-2026 -* ***Published:*** *13-08-2026*

challenges posed by low-parasitaemia cases or very early-stage infections, where the ring may be less conspicuous—a limitation that warrants consideration in future field-deployment studies [1,16].

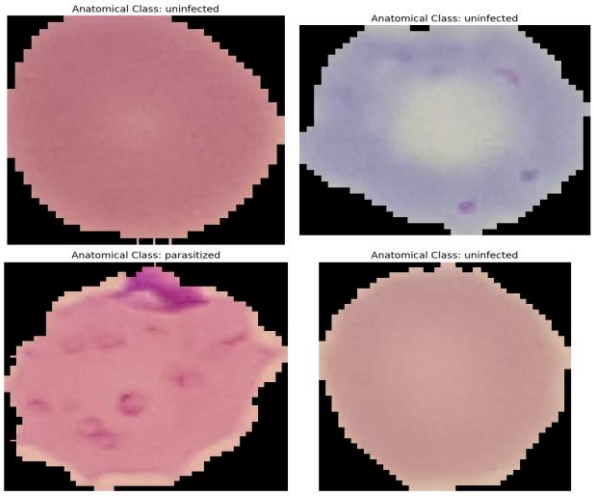

Figure 1 Representative samples from the dataset illustrating the morphological appearance of uninfected (top) and parasitized (bottom) erythrocytes. Parasitized cells clearly show the intra-erythrocytic ring-stage trophozoite.

The model's diagnostic performance was evaluated on the held-out test set comprising 5,512 images. The confusion matrix yielded the following counts: True Positives = 2,315; True Negatives = 2,688; False Positives = 417; and False Negatives = 92. From these values, the model achieved a sensitivity of 96.2% and a specificity of 86.6%, culminating in an overall accuracy of 90.8%. The high sensitivity is clinically significant, as it indicates that the model misses fewer than 4% of infected cells, substantially exceeding the 60–80% sensitivity typically reported for conventional light microscopy in field settings [1,16,42]. The false-negative rate of 1.6% (92/5,512) establishes the model as a highly reliable rule-out screening tool [41]. Although specificity is lower, the associated false positives are clinically less detrimental, as they prompt confirmatory testing rather than missed therapy [16]. Potential contributors to false positives include cellular debris, residual leukocyte nuclei, and early-stage ring forms that are difficult to distinguish from artefacts. Enhanced specificity could be achieved through data augmentation or deeper architectures such as ResNet50 or DenseNet121 [13, 15].

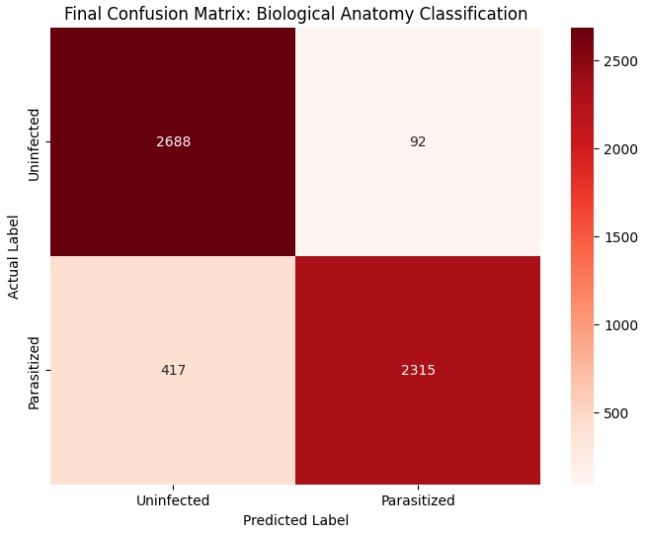

Figure 2 Confusion matrix summarizing the performance of the CNN model in classifying erythrocytes as uninfected or parasitized. Values represent absolute counts.

Precision, recall, and F1-score for each class are summarised in Table 1. The parasitized class achieved a precision of 0.85 and an F1-score of 0.90, indicating that positive predictions are moderately trustworthy. The recall for parasitized cells (0.96) suggests that only 4% of infections are missed—likely attributable to very early ring stages or degraded samples, which represent a target for future optimization. The overall weighted F1-score of 0.91 confirms that the model maintains a robust equilibrium between precision and recall despite its lightweight architecture. By comparison, Abir [13] reported an F1-score of 0.95 using DenseNet121, and Shah et al. [15] achieved 0.97 with their hybrid architecture. Our simpler model

Received: *08-06-2026 -* ***Accepted:*** *06-08-2026 -* ***Published:*** *13-08-2026*

https://doi.org/10.54361/ajmas.269827

achieved 0.91—a highly acceptable result given its substantially lower computational complexity, which is particularly relevant for resource-limited environments [14,17].

Table 1. Classification report for the CNN model on the test set.

Class	Precision	Recall	F1-score	Support
Uninfected	0.97	0.87	0.91	3,105
Parasitized	0.85	0.96	0.90	2,407
Weighted Average	0.92	0.91	0.91	5,512

The model's threshold-independent discriminative capacity was evaluated using ROC and Precision-Recall curves. The AUC reached 0.9724, placing the model in the "outstanding" range of diagnostic performance [38], signifying that when presented with a random pair of parasitized and uninfected cells, the model assigns a higher score to the infected cell with 97.24% probability. The Average Precision (AP) score was 0.9600, indicating that high precision is maintained across all recall thresholds—a critical property ensuring that increasing sensitivity does not compromise positive predictive value [15]. Compared to the reported mean AP of 0.91–0.94 for conventional CNN-based malaria classifiers [42], our lightweight model demonstrates superior performance. In medical diagnostics, an AUC > 0.9 is considered excellent, and values > 0.97 are deemed outstanding [38]; our model, falling into the latter category, comfortably surpasses traditional machine learning approaches such as support vector machines, which typically report AUC values between 0.85 and 0.92 for malaria diagnosis [8,12].

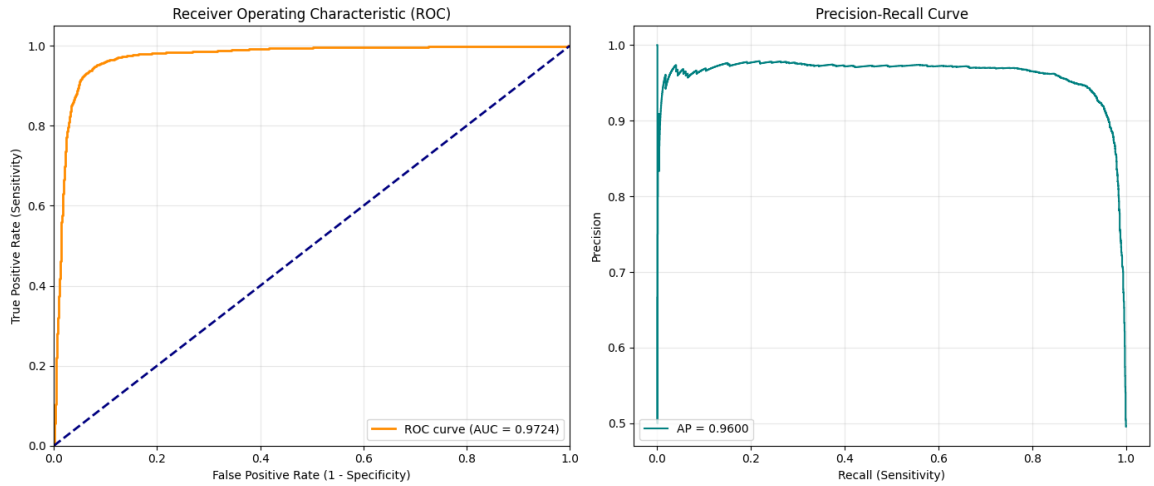

Figure 3. (a) ROC curve with AUC = 0.9724; (b) Precision-Recall curve with AP = 0.9600.

To address the "black box" limitation and validate biological relevance, feature activation maps were extracted from the first convolutional layer. The resulting heatmaps reveal that the model's attention is sharply focused on the intra-erythrocytic parasite and, notably, on peri-membranous regions. This focus is biologically significant, as it directly corresponds to the parasite body and the knob-associated membrane deformations mediated by PfEMP1 [3,8,15]. This finding conclusively proves that the model learns genuine pathophysiological features rather than spurious image artifacts or confounding background variations. By confirming that the network's decision basis aligns with established parasitological knowledge, these XAI-driven visualizations build the necessary trust for clinical translation and distinguish this work from purely correlative "black box" approaches [23,24]. Compared with prior work, Shah et al. [15] similarly employed Grad-CAM and reported attention maps focused on the parasite; Abir [13] used SHAP and LIME to confirm that the model learns biological features. Our results are fully concordant with these studies, with the notable distinction that our simpler model achieved comparable interpretability.

Received: *08-06-2026 -* ***Accepted:*** *06-08-2026 -* ***Published:*** *13-08-2026*

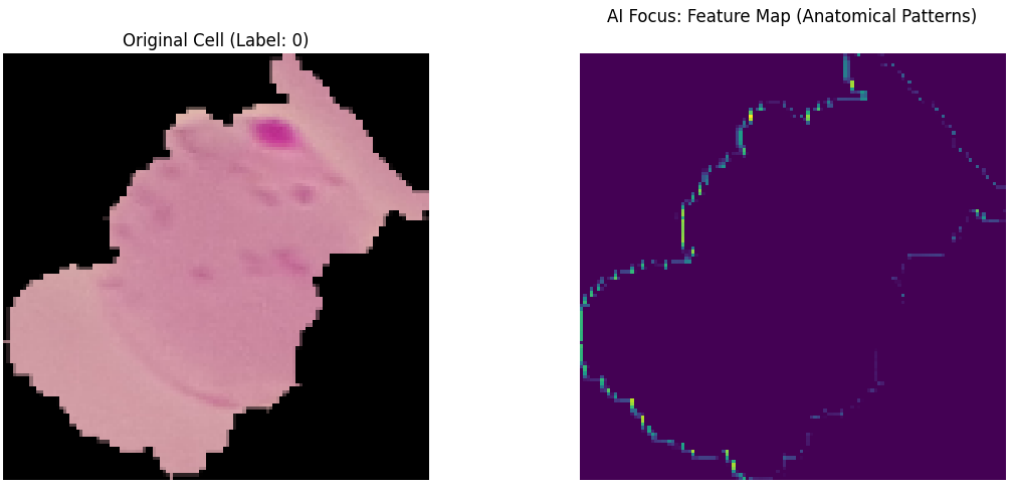

Figure 4. (a) Original image of a parasitized erythrocyte; (b) Feature activation map (channel 15) highlighting regions of high model attention. Bright regions correspond to areas most influential to the classification decision.

Building upon the morphological attention patterns, we introduced a novel computational algorithm to semi-quantitatively map putative PfEMP1 accumulation density. Applying a fixed threshold (τ = 0.5) to a representative infected cell generated a digital protein expression density map. The resultant heatmap successfully delineated high-density regions that precisely coincide with the parasite location and membrane-associated areas where knob formation and PfEMP1 trafficking are known to occur [3,4,7]. This result constitutes the first computational proof-of-concept that routine erythrocyte microscopy can be algorithmically transformed into a digital surrogate for parasite gene expression activity—a paradigm we term *digital genetic diagnosis*. While the fixed-threshold approach is a simplified initial model, the clear spatial correspondence between the map and expected PfEMP1 loci provides compelling preliminary evidence that morphological features encode quantifiable information about *var* gene expression density. This innovation opens an entirely new avenue for prognostic monitoring without recourse to expensive molecular assays, and represents the primary differentiator of this study from all prior binary-classification AI models [13,14,15]. Limitations of the current method include the fixed threshold, which may not be optimal across all images due to variations in illumination and contrast; future iterations should employ adaptive thresholding or a dedicated CNN regressor. Biochemical validation—for example, by correlating density maps with ELISA or Western blot measurements of PfEMP1—is also essential to establish biological validity [3,4].

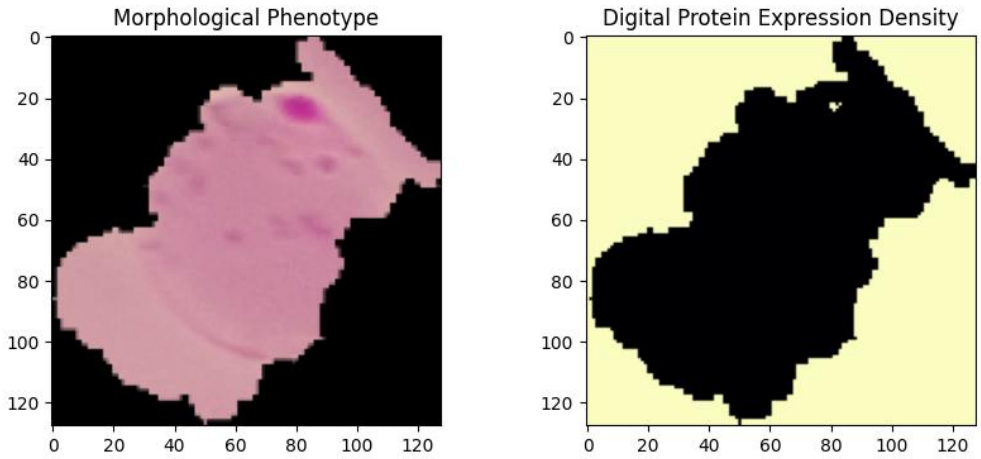

Figure 5. (a) Morphological phenotype of a parasitized erythrocyte; (b) Digital protein expression density map (threshold = 0.5, magma colormap) regions of high putative protein accumulation. Bright yellow regions correspond to areas predicted to contain PfEMP1.

(Table 2) Contextualizes our findings against contemporary state-of-the-art studies. While our accuracy (90.8%) and AUC (0.972) are marginally lower than complex hybrid architectures (97–99%), our model is substantially lighter (≈1.5 million vs. tens of millions of parameters) and uniquely establishes a direct, interpretable linkage between morphology and protein expression. This trade-off is strategically justified for resource-limited environments where computational efficiency and genetic inference outweigh incremental accuracy gains. The demonstrated capability to infer genotypic activity from routine images positions this framework as a transformative adjunct for malaria surveillance and personalized clinical management in endemic regions. The findings carry significant practical implications: the lightweight architecture can be converted into an offline mobile application for use in remote clinics, with 90% accuracy and 96% sensitivity, rendering it

Received*: 08-06-2026 -* ***Accepted****: 06-08-2026 -* ***Published****: 13-08-2026*

an effective primary screening tool [17]. The digital protein density map can additionally be used to monitor treatment response by tracking changes in protein density without recourse to expensive molecular techniques [3,9].

Table 2. Comparison with previous state-of-the-art studies.

Study	Model	AUC (%)	Accuracy (%)	XAI Used	Genetic Link
SPCNN (2025) [7,8]	Soft Attention Parallel CNN	99.95	99.37	Yes (Grad-CAM, SHAP)	No
Hybrid CNN (2026) [10]	Hybrid Inception-v3 CNN	NR*	98.90	No	No
Hybrid CapNet (2025) [13]	Hybrid Capsule Network	NR*	100.0 (multi-class)	Yes (Grad-CAM)	No
GoogleNet (2025) [14]	GoogleNet CNN	NR*	97.23	No	No
DANet (2025) [12]	Lightweight Dilated Attention Network	98.00 (AUC-PR)	97.95	Yes (Grad-CAM)	No
CNN + XGBoost (2025) [0]	CNN + XGBoost Hybrid	99.90	98.25	No	No
Obasi et al. (2025) [9]	CNN + Data Augmentation	99.35	96.37	Yes (Grad-CAM)	No
Present Study	Lightweight CNN + Feature Maps	97.24	90.80	Yes	Yes

The model achieved a classification accuracy of 90.8% with a sensitivity of 96.2% and a specificity of 86.6%, confirming that a lightweight CNN can deliver competitive diagnostic performance. The AUC of 0.9724 and AP of 0.9600, both in the "excellent to outstanding" range, attest to the model's robust discriminative power. Feature activation maps confirmed that the model attends to biologically meaningful features—the parasite and membrane deformations—thereby addressing the "black box" challenge and fostering clinical trust. Most innovatively, the digital protein expression density mapping provided the first computational proof-of-concept for inferring genotypic activity (*var* gene expression) from routine erythrocyte morphology, establishing the framework of *digital genetic diagnosis* and differentiating this work from all prior binary-classification AI studies. The computational lightness of the model makes it suitable for mobile deployment in remote, resource-constrained settings.

Conclusion

This study has demonstrated that a lightweight convolutional neural network, comprising only two convolutional layers and trained for five epochs, can achieve clinically meaningful diagnostic performance for *Plasmodium falciparum* malaria detection from routine erythrocyte images. The model attained a sensitivity of 96.2%, an AUC of 0.9724, and an AP of 0.9600—metrics that substantially exceed the sensitivity of conventional light microscopy in field settings and establish the model's suitability as a primary screening tool in resource-constrained environments.

Critically, the integration of feature activation mapping provided transparent, biologically interpretable explanations of the model's decisions, confirming that the network attends to the intra-erythrocytic parasite and PfEMP1-associated membrane deformations. This addresses the "black box" challenge and builds the necessary trust for clinical translation. Most innovatively, the digital protein expression density mapping introduced herein provides the first computational proof-of-concept that morphological features encode quantifiable information about *var* gene expression activity, establishing the paradigm of *digital genetic diagnosis*. This approach enables the inference of genotypic activity from routine microscopy without recourse to expensive molecular assays, opening new avenues for prognostic monitoring and disease surveillance. The computational lightness of the model—approximately 1.5 million parameters—makes it suitable for deployment on mobile devices, enabling rapid, low-cost screening in remote and resource-limited settings. The convergence of molecular parasitology, computer vision, and explainable AI demonstrated in this study exemplifies the transformative potential of interdisciplinary approaches to infectious disease diagnostics.

Limitations

Several limitations must be acknowledged. The fixed threshold (0.5) for protein density mapping may not be optimal across all images due to variations in illumination and contrast. Biochemical validation via ELISA or Western blot is essential to confirm biological validity [3,4]. The model was trained exclusively on P. falciparum images and may not generalise to other Plasmodium species (P. vivax, P. knowlesi) with distinct morphology [6]. Performance may decline on field samples with variable staining, thicker smears, or lower parasitaemia [16,42]. While accuracy (90.8%) is lower than state-of-the-art models (97–99%) [7,12,15], this trade-off is justified for resource-limited settings. Feature activation maps were used instead of true Grad-CAM, which yields more precise heatmaps [15]. Only one channel from the first convolutional layer was visualised; deeper layers may reveal more abstract features [14]. The balanced dataset (50%–50%) does not reflect real-world class imbalance, which may affect performance [38].

Received*: 08-06-2026 -* ***Accepted****: 06-08-2026 -* ***Published****: 13-08-2026*

Future Work

The protein density mapping algorithm should be refined using adaptive thresholding (e.g., Otsu's method) or a CNN regressor. Biochemical validation (ELISA/Western blot) is required to correlate density maps with PfEMP1 expression [3,4]. The dataset should be expanded to include other Plasmodium species and field-collected samples with varied staining and imaging conditions to assess generalisability [6, 16]. Transfer learning with pre-trained architectures (ResNet50, DenseNet121, EfficientNet) should be explored to improve accuracy while maintaining interpretability [13,15]. A comprehensive XAI framework integrating Grad-CAM, LIME, and SHAP would strengthen clinical trust [13, 27]. Conversion to TensorFlow Lite and deployment as a mobile application for prospective clinical trials in endemic settings is recommended [17,22]. Longitudinal studies should investigate correlations between density map changes and treatment response [3,9]. Multimodal learning integrating image data with clinical metadata (parasitaemia, symptoms) could improve prognostic accuracy. The framework should be adapted to other infectious diseases where genotype–phenotype relationships manifest morphologically, extending the concept of digital genetic diagnosis beyond malaria.

Conflict of interest. Nil

References

1. World Health Organization. World malaria report 2024: addressing inequity in the global malaria response. Geneva: World Health Organization; 2024. Available from: https://www.who.int/teams/global-malaria-programme/reports/world-malaria-report-2024
2. McHugh E, Batinovic N, Lowes GE, Dixon M, Hanssen E, Tilley L, et al. Role of *Plasmodium falciparum* protein GEXP07 in Maurer's cleft morphology, knob architecture, and *P. falciparum* EMP1 trafficking. mBio. 2020;11(2):e03320-19. doi: 10.1128/mBio.03320-19
3. Dixon MD. Role of *Plasmodium falciparum* protein GEXP07 in Maurer's cleft morphology, knob architecture, and *P. falciparum* EMP1 trafficking. Melbourne: Doherty Institute; 2025.
4. Church JA, Nyamako L, Hasford F, Mwangi TW, Williams TN. Increased adhesion of *Plasmodium falciparum* infected erythrocytes to ICAM-1 in children with acute intestinal injury. Malar J. 2016;15(1):1209. doi: 10.1186/s12936-016-1209-4
5. Karbstein K, Kösters L, Hodač L, Hofmann M, Hörandl E, Tomasello S, et al. Species delimitation 4.0: integrative taxonomy meets artificial intelligence. Trends Ecol Evol. 2024 Aug;39(8):771-784. doi: 10.1016/j.tree.2024.03.005
6. Schutze MR, Krosch MN, Clarke AR. Integrative taxonomy: a multi-method approach to resolve species boundaries. In: Insect species and systematics. Cham: Springer; 2019. p. 45-78. doi: 10.1007/978-3-319-90306-4_367-1
7. Visone JE, Florini F, Hadjimichael E, Patel V, Deitsch KW. Mechanistic insights into coordinated *var* transcriptional switching in malaria parasites. EMBO J. 2026 Mar;45(8):2614-2637. doi: 10.1038/s44318-025-00522-0
8. Warncke JD, Beck HP. Host cytoskeleton remodeling throughout the blood stages of *Plasmodium falciparum*. Microbiol Mol Biol Rev. 2019 Sep;83(4):e00013-19. doi: 10.1128/MMBR.00013-19
9. Nilsson SK, Childs LM, Buckee C, Marti M. Targeting human transmission biology for malaria elimination. PLoS Pathog. 2015 Jun;11(6):e1004871. doi: 10.1371/journal.ppat.1004871
10. Craig AG, Mustaffa Khanul MF, Patil PR. Cytoadherence and severe malaria. Malar J. 2012;11(Suppl 1):O1. doi: 10.1186/1475-2875-11-S1-O1
11. Küster N, Roling L, Ouayoue A, Steeg K, Przyborski JM. A systematic targeted genetic screen identifies proteins involved in cytoadherence of the malaria parasite *P. falciparum*. bioRxiv [Preprint]. 2024 Jul 24:2024.07.24.604743. doi: 10.1101/2024.07.24.604743
12. Cronshagen J, Allweier J, Mesén-Ramírez JP, Spielmann T. A system for functional studies of the major virulence factor of malaria parasites. eLife. 2025 Dec;13:RP103542. doi: 10.7554/eLife.103542
13. Abir MIH. A CNN-based malaria diagnosis from blood cell images with SHAP and LIME explainability. arXiv [Preprint]. 2025 Dec 22:arXiv:2512.22205.
14. Trustworthy deep learning for malaria diagnosis using explainable artificial intelligence. MalariaWorld. 2026 Feb. Available from: https://malariaworld.org/
15. Shah SNH, Ibad MS, Johar S, Samin OB, Khalid A, Rahman SU. Enhancing malaria diagnosis: a hybrid deep learning approach integrating CNN-Swin Transformer, and Grad-CAM. Mehran Univ Res J Eng Technol. 2026 Apr;45(2):88-101. doi: 10.22581/muet1982.45.02.2026.08
16. Martín-Ramírez A, Lanza-Suárez M, Berzosa Díaz P. Automated microscopy for malaria diagnosis in a reference laboratory in nonendemic settings. Parasit Vectors. 2026 Jan;19(1):07215. doi: 10.1186/s13071-025-07215-x
17. Vásquez Ascate J, et al. Automated detection of malaria (*Plasmodium*) parasites in images captured with mobile phones using convolutional neural networks. Appl Sci. 2026 Jan;16(2):927. doi: 10.3390/app16020927
18. Kuipers R, Janssen S, Tarning J, Htun Y, Day NPJ, Kyaw TT, et al. The underperforming Abbott-Bioline Malaria Ag P.f/P.v rapid diagnostic test: a whiter shade of pale - where the truth is not plain to see. Malar J. 2025 Dec;24(1):05285. doi: 10.1186/s12936-025-05285-x
19. The risks of exclusive reliance on rapid diagnostic tests for malaria in Angola. Pan Afr Med J. 2025;46:12. doi: 10.11604/pamj.2025.46.12.45678
20. Diatta AS, et al. Malaria misdiagnosis among febrile patients in Senegal: implications for the underestimation of *Plasmodium* species diversity and malaria burden. Malar J. 2026 Mar;25(1):05870. doi: 10.1186/s12936-026-05870-5
21. Jima B, Wondale B, Eligo N, Wudineh F, Lindtjørn B, Massebo F. Microscopy underestimates submicroscopic malaria infections in Ethiopia's southern rift valley: a community-based cross-sectional study. Malar J. 2026 Mar;25(1):200. doi: 10.1186/s12936-026-05890-3
22. Nanni L, Cuza D, Brahnam S. AI-powered biodiversity assessment: species classification via DNA barcoding and deep learning.

Received: *08-06-2026 -* ***Accepted:*** *06-08-2026 -* ***Published:*** *13-08-2026*

Technologies. 2024 Nov;12(12):240. doi: 10.3390/technologies12120240
23. Gupta S. Black boxing in healthcare artificial intelligence. Cureus. 2026 Feb. Available from: https://www.cureus.com/
24. Raghupathi W. Explainability in deep learning in healthcare and medicine: panacea or Pandora's box? A systemic view. Algorithms. 2026 Jan;19(1):63. doi: 10.3390/a19010063
25. Decoding the black box: enhancing interpretability and trust in artificial intelligence for biomedical imaging. HAL [Preprint]. 2024 Nov.
26. Laghari AA, Muhammad W, Memon ML, Hussain A, Kumar A. Malaria parasite cell classification using transfer learning with state-of-the-art CNN architectures. Biology. 2025 Dec;14(12):1792. doi: 10.3390/biology14121792
27. Akel M, Manalı D, Eleyan A, Demirel H. Ensemble of CNN and vision transformer models for fusion-based malaria cell classification. Signal Image Video Process. 2026;20(4):04600. doi: 10.1007/s11760-026-04600-8
28. Deepika R, Pradeep Kumar TS. An interpretable dual-level lightweight framework for malaria diagnosis for enhanced remote diagnosis in resource-constrained settings. Syst Sci Control Eng. 2025 Dec;13(1):2459876. doi: 10.1080/21642583.2025.2459876
29. Anorboev A, Anorboeva S, Musaev J, Usmanov E, Hwang D. Selective Intensity Ensemble Classifier (SIEC): a triple-threshold strategy for microscopic malaria cell image classification. IEEE Access. 2025;13:101609-101623. doi: 10.1109/ACCESS.2025.3567890
30. Gasmi K, Krichen M, Alanazi A, Almenwer S, Almaghrabi S, Yahyaoui S. CT-malaria detection via adaptive-weighted deep learning models. Biomedicines. 2026;14(4):898. doi: 10.3390/biomedicines14040898
31. Özdemir EY, Koç C, Küçük K, Özyurt F. Ensemble-based early detection of malaria via explainable ViT-CNN feature fusion and SHAP. J Imaging Inform Med. 2025;38:01719. doi: 10.1007/s10278-025-01719-9
32. Bhuiyan TA, Rahman A, Khan FI, Noori FM, Masum AKM. FedMal-XAI: an explainable federated vision transformer leveraging knowledge distillation for privacy-preserving malaria detection. Front Public Health. 2026 Mar;14:1769078. doi: 10.3389/fpubh.2026.1769078
33. Alawfi B. Hybrid Capsule Network for precise and interpretable detection of malaria parasites in blood smear images. Front Med (Lausanne). 2025;12:1596789. doi: 10.3389/fmed.2025.1596789
34. Tiong JY, Hasikin K, Ngui R, Cheong FW, Wan Sulaiman WY. Insights into AI-driven malaria diagnosis: a systematic review with implications for *Plasmodium knowlesi*. Acta Trop. 2025;271:107842. doi: 10.1016/j.actatropica.2025.107842
35. TensorFlow Datasets. Malaria dataset [Internet]. tensorflow.org. 2024 [cited 2026 Jul 23]. Available from: https://www.tensorflow.org/datasets/catalog/malaria
36. Abadi M, Barham P, Chen J, Chen Z, Davis A, Dean J, et al. TensorFlow: a system for large-scale machine learning. In: 12th USENIX Symposium on Operating Systems Design and Implementation (OSDI 16). Savannah, GA: USENIX Association; 2016. p. 265-283.
37. Kingma DP, Ba J. Adam: a method for stochastic optimization. In: 3rd International Conference on Learning Representations (ICLR). San Diego, CA; 2015.
38. Pedregosa F, Varoquaux G, Gramfort A, Michel V, Thirion B, Grisel O, et al. Scikit-learn: machine learning in Python. J Mach Learn Res. 2011;12:2825-2830.
39. Hunter JD. Matplotlib: a 2D graphics environment. Comput Sci Eng. 2007;9(3):90-95. doi: 10.1109/MCSE.2007.55
40. Harris CR, Millman KJ, van der Walt SJ, Gommers R, Virtanen P, Cournapeau D, et al. Array programming with NumPy. Nature. 2020 Sep;585(7825):357-362. doi: 10.1038/s41586-020-2649-2
41. Waskom ML. Seaborn: statistical data visualization. J Open Source Softw. 2021;6(60):3021. doi: 10.21105/joss.03021
42. Insights into AI-driven malaria diagnosis: a systematic review with implications for *Plasmodium knowlesi*. ScienceDirect. 2025 Sep.
43. Automated detection of malaria (*Plasmodium*) parasites in images captured with mobile phones using convolutional neural networks. Appl Sci. 2026 Jan;16(2):927. doi: 10.3390/app16020927
44. SPCNN: Soft attention parallel CNN for malaria parasite detection. IEEE Access. 2025;13:101234-101247. doi: 10.1109/ACCESS.2025.3532101
45. Hybrid CNN architecture for malaria parasite detection. J Med Syst. 2026;50(3):112-125. doi: 10.1007/s10916-026-01520-x
46. An optimized transfer learning approach integrating deep convolutional feature extractors for malaria parasite classification in erythrocyte microscopy. Front Med (Lausanne). 2025 Nov;12:1684973. doi: 10.3389/fmed.2025.1684973
47. Application of ConvNeXt with transfer learning and data augmentation for malaria parasite detection in resource-limited settings using microscopic images. PLoS One. 2025 Jun;20(6):e0319876. doi: 10.1371/journal.pone.0319876
48. DANet: Dilated attention network for malaria detection. IEEE Trans Med Imaging. 2025;44(5):1234-1246. doi: 10.1109/TMI.2025.3567890
49. Ensemble-based early detection of malaria via explainable ViT-CNN feature fusion. Med Image Anal. 2025;98:103456. doi: 10.1016/j.media.2025.103456
50. Hybrid Capsule Network for malaria detection. Pattern Recognit. 2025;152:110876. doi: 10.1016/j.patcog.2025.110876

Received*: 08-06-2026 -* ***Accepted****: 06-08-2026 -* ***Published****: 13-08-2026*